BIOMIMETICS

An 88-milligram insect-scale autonomous crawling robot driven by a catalytic artificial muscle

Xiufeng Yang*, Longlong Chang, Néstor O. Pérez-Arancibia*

The creation of autonomous subgram microrobots capable of complex behaviors remains a grand challenge in robotics largely due to the lack of microactuators with high work densities and capable of using power sources with specific energies comparable to that of animal fat (38 megajoules per kilogram). Presently, the vast majority of microrobots are driven by electrically powered actuators; consequently, because of the low specific energies of batteries at small scales (below 1.8 megajoules per kilogram), almost all the subgram mobile robots capable of sustained operation remain tethered to external power sources through cables or electromagnetic fields. Here, we present RoBeetle, an 88-milligram insect-sized autonomous crawling robot powered by the catalytic combustion of methanol, a fuel with high specific energy (20 megajoules per kilogram). The design and physical realization of RoBeetle is the result of combining the notion of controllable NiTi-Pt–based catalytic artificial micromuscle with that of integrated millimeter-scale mechanical control mechanism (MCM). Through tethered experiments on several robotic prototypes and system characterization of the thermomechanical properties of their driving artificial muscles, we obtained the design parameters for the MCM that enabled RoBeetle to achieve autonomous crawling. To evaluate the functionality and performance of the robot, we conducted a series of locomotion tests: crawling under two different atmospheric conditions and on surfaces with different levels of roughness, climbing of inclines with different slopes, transportation of payloads, and outdoor locomotion.

INTRODUCTION

Biological machines still surpass their robotic counterparts in almost every aspect, including power conversion, actuation, sensing, and control. The most advanced insect-scale microrobots, for instance, have yet to achieve the capabilities observed in honeybees and beetles. No subgram robot has been reported to autonomously complete tasks that are challenging or useful for humans, and the vision of creating truly autonomous artificial insects will become a reality only once several of the long-standing grand challenges in robotics are overcome (*1*). Namely, new methods for microfabrication, actuation, and control must be developed along with the introduction of new sources of power, mechanisms, structural microcomponents, and actuation materials (*1*, *2*). Here, we understand autonomy as the capability of a robot to perform sustained and periodic operations without being tethered to external power sources or controllers through cables or wireless fields. From this perspective, despite impressive recent results (*3*–*5*), progress toward full autonomy at the subgram scale has been hindered by the lack of actuation methods capable of using sources of power with high energy densities (HEDs). This issue arises because electricity is the most common type of power used to drive microrobots (*6*–*14*) and, therefore, for which the only path to autonomy is the use of batteries. The limitations of state-of-the-art batteries become evident when their specific energies and/or sustainable power outputs are compared to those of the fat metabolized by insects (~38 MJ/kg; ~5.2 mW) (*15*). For example, the best centimeter-scale Li-ion batteries exhibit specific energies in the order 1.8 MJ/kg (*16*).

Most insects have strong muscles for intense activity (*17*) and stout bodies for energy storage in the form of fat and glycogen (*18*); inspired by the metabolism of these animals, we developed reliable and mechanically robust artificial micromuscles with both high work densities (HWDs) and the capability of using HED sources of power (2H). To demonstrate this approach, we developed RoBeetle, an autonomous crawling robot that weighs only 88 mg excluding fuel; during operation, the weight of the robot can vary from 88 mg (empty tank) to 183 mg (full tank). The principal innovation that enabled this development is the use of controlled catalytic combustion to thermally excite, according to a periodic pattern, a wire composite with a NiTi shape-memory alloy (SMA) core and a surface made of platinum (Pt) that acts as a catalyst. This technique can be implemented using different fuels, including hydrogen (H_2), methanol (CH_3OH), propane (C_3H_8), and butane (C_4H_{10}). In this case, we use methanol, which has a specific energy of about 20 MJ/kg and can be stored as a liquid at the atmospheric pressure. A key element that makes the proposed approach possible is feedback control of the catalytic combustion process, according to a scheme in which the periodic deformation of the SMA material is used to indirectly sense temperature by using an identified model of the hysteretic dynamics of the wire and, also, to synchronously open and close the microvalves that modulate the flow of fuel. Thus, the controller is implemented onboard using only mechanical components embedded in the artificial muscle mechanism. This control strategy enables the autonomous operation of RoBeetle in a sustained manner, which is the most distinct characteristic of this system with respect to other mechanisms powered by HED sources.

In the context of energy conversion, the notion of harnessing the heat released by catalytic reactions to drive thermally excitable materials has been discussed in the past. For example, the work in (*19*), using a commercial dynamic mechanical analyzer, demonstrated that the catalytic combustion of H_2 can be used to excite the strain response of a catalyst-coated SMA wire at low frequency (~0.003 Hz) in open loop, and a perspective regarding the potentials of this method is presented in (*20*). Furthermore, the idea of integrating power, actuation, sensing, and control into self-contained

Department of Aerospace and Mechanical Engineering, University of Southern California, Los Angeles, CA 90089-1453, USA.
*Corresponding author. Email: xiufeng@usc.edu (X.Y.); perezara@usc.edu (N.O.P.-A.)

mechanical systems is centuries old, and this approach was used in numerous cases before the advent of the electronics era—the most notable example being the centrifugal governor (*21*). Contemporary examples of this approach are the electronics-free localized controllers presented in (*22*) and the SMA-based mechanisms that are activated by direct atmospheric temperature variations to open and close greenhouse windows in (*23*). The main innovations that made the development of RoBeetle possible are a novel design and the associated microfabrication method that enabled us to embed an entire electronics-free mechanical control mechanism (MCM) into the microrobot, thus satisfying stringent size, weight, and energy constraints that are not achievable using microbatteries (*16*, *24*) or other mechanical-based techniques such as those in (*25*) and (*26*). As in the cases of other recently developed microrobots (*3*, *5*, *27*), RoBeetle is entirely fabricated using the smart composite microstructure (SCM) method in (*28*).

RESULTS

Catalytic artificial muscles for microrobotic actuation

To create 2H microactuators capable of driving insect-scale robots, we combined the HEDs of fuels (Fig. 1A) with the HWDs of SMAs (Fig. 1B). The main component of the actuation mechanism is the artificial muscle depicted in Fig. 2A, which is composed of a NiTi core and an outer catalytic layer of agglutinated Pt powder. During operation, the SMA core of the composite wire is excited by the heat produced by the controlled catalytic combustion of fuel on the catalytic surface; for example, in Fig. 2A, the reaction $CH_3OH(g) + 3/2\,O_2(g) \xrightarrow{Pt} 2H_2O(g) + CO_2(g)$ (catalytic combustion of methanol) is facilitated by the Pt catalyst to produce the heat required to excite the SMA material according to the shape-memory effect (SME) depicted in Fig. 2B (see text S1 for details). Namely, the catalytic combustion of CH_3OH raises the temperature of the NiTi material beyond the point required to transition from a martensite to an austenite phase when fuel is delivered to the catalytic surface of the NiTi-Pt composite wire, and contraction occurs. Conversely, when the flow of fuel is stopped and the chemical reaction is suspended, the SMA material cools down and the wire extends, thus transitioning from an austenite to a martensite phase. In this way, by regulating the flow of fuel according to a periodic pattern and simultaneously maintaining an appropriate tension, the composite wire produces a periodic actuation output.

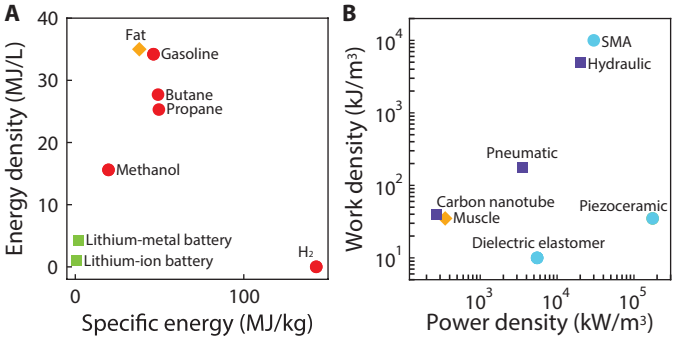

Fig. 1. Energy sources and actuation methods for microactuation. (**A**) Energy densities and specific energies of various power sources (see table S1 for detailed data). The red circles indicate potential energy sources to power the proposed NiTi-Pt–based artificial muscles as these fuels can be used in exothermic reactions catalyzed by Pt. Fat, the type of energy used by animals, is represented with a yellow diamond. Batteries are indicated with green squares. (**B**) Work and power densities of different actuation methods (see table S2 for detailed data). The blue circles indicate the actuators that have been used in microrobotic applications, and the purple squares represent those that have not been used in microrobotics. The yellow diamond indicates the properties of animal muscle.

A scanning electron microscope (SEM) image of the surface of a NiTi-Pt composite wire, fabricated using the method described in Materials and Methods and fig. S1, is shown in Fig. 2 (C to E). The catalytic surface at the microscopic level is not homogeneous because the fabrication method creates three-dimensional (3D) structures composed of particles of Pt-black randomly agglomerated together. This surface pattern creates a catalytically active area about 2200 times larger than that of the bare NiTi wire, which is essential to achieving sustained and controllable catalytic combustion. Using the information provided by the manufacturer of the Pt-black, we estimate that the resulting catalytic specific surface area is ~27 m^2/g. Consistent with our own experimental observations, earlier work indicates that Pt coating based on the agglutination of particles produces highly active catalytic surfaces (*29*, *30*).

To characterize the thermomechanical behavior of the NiTi-Pt–based artificial muscle for the purpose of controller synthesis, we constructed an experimental setup capable of precisely controlling the flow and delivery of gases to the catalytic surface, whereas sensing the temperature of the outer layer of the composite wire, precisely measuring the strain output, and regulating the total load applied to the SMA material (further details are presented in text S2). Obtaining an accurate model of the complex nonlinear strain-temperature-stress dynamical behavior of an artificial muscle, including the relationship between superelasticity and the SME (*31*), is difficult. Therefore, using the methods in (*32*, *33*), we identify the temperature-strain hysteretic behavior of the NiTi-Pt composite wires under the constant stress of 164 MPa, a value close to the average stress experienced by the actuator that drives the RoBeetle prototype during operation. This process of system identification is an essential component of the robotic design procedure as the transition temperatures of the SMA material are among the most important parameters that determine the dynamics of the system; details are provided in the next section.

Figure 2F shows the identified major loop and two eccentric minor loops, for a stress of 164 MPa, associated with the 9.8-mm-long NiTi-Pt wire used to drive the RoBeetle prototype. A major loop refers to the heating-cooling cycle during which the SMA material undergoes a complete phase transition from a martensitic state to an austenitic state and, then, completely back to a martensitic state. Consistently, in this particular case, a minor loop refers to the heating-cooling cycle during which the SMA material undergoes a partial phase transition from a martensitic state to an austenitic state and, then, back to the initial martensitic state. From the hysteretic temperature-strain curve of the major loop, it can be deduced that the artificial muscle is capable of producing a maximum strain of about 3% when heated up to 154.5°C and, then, it recovers its original length when cooled down to the room temperature (~25°C). According to widely used constitutive models (*34*, *35*), constant-stress major loops can be characterized by four critical transition temperatures (see text S1 for detailed definitions)—namely, from low to high: T_{mf} = 58°C, T_{ms} = 70°C, T_{as} = 87°C, and T_{af} = 99°C, as indicated in Fig. 2F.

The sequential completion of major loops generates a periodic output strain with the maximum amplitude achievable by the wire

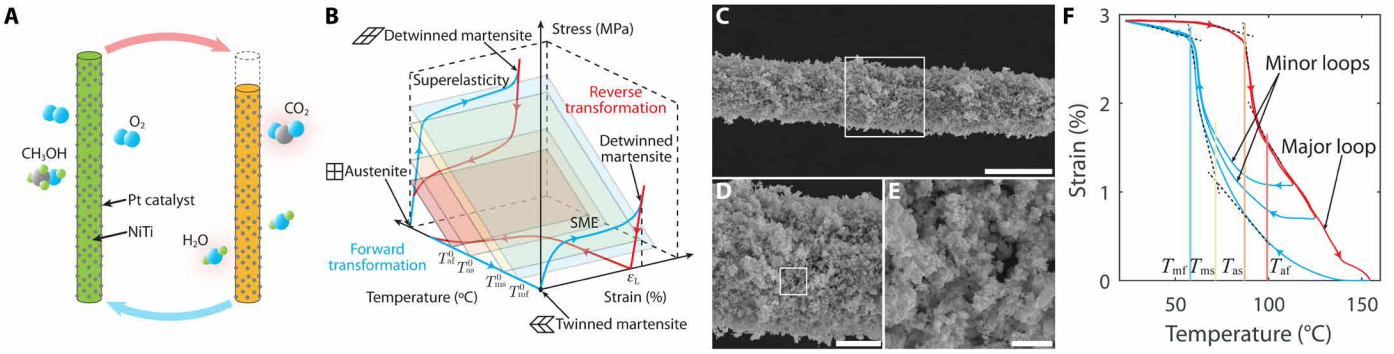

Fig. 2. Catalytic artificial muscle. (**A**) Diagram of a NiTi-Pt composite wire. As the wire is exposed to the reactants, CH_3OH and O_2, it heats up and contracts due to the exothermic reaction facilitated by the Pt catalyst; when the fuel supply is stopped, the wire cools down and extends to its original length. Periodic actuation is generated by repeating this process. (**B**) Generic strain-temperature-stress diagram of a NiTi SMA wire. The phase transitions between austenite and martensite states are characterized by hysteretic loops associated with the SME and superelasticity (*34*, *35*). The relationship between a constant stress value and the parameters of a loop are depicted using four colored planes. For further details, see text S1. (**C** to **E**) SEM images of the surface of a NiTi-Pt wire with a diameter of 87 μm. The rough and porous catalytic layer (Pt-black) has a thickness of ~18.1 μm. The magnifications of the images are ×350, ×1200, and ×6500; the scale bars indicate distances of 100, 30, and 5 μm, respectively. (**F**) Experimental strain-temperature hysteretic relationship of a NiTi-Pt composite wire, obtained under constant stress. We show a major loop and two eccentric minor loops. The corresponding temperature and strain signals are shown in fig. S2.

at a given constant stress. Note, however, that to operate following the trajectory of a major hysteretic cycle is not necessarily optimal from the perspectives of speed and/or energy. For example, as shown in Fig. 2F, comparatively large output strains can be obtained, with the same reaction rates as those used to induce a major loop, by exciting the SMA material with temperatures within a relatively narrow range. Accordingly, we can make the actuation of a RoBeetle prototype efficient by controlling the catalytic reactions on the surface of the NiTi-Pt wire such that the corresponding temperature oscillates between T_{mf} and T_{af}, which corresponds to a minor loop. In static experiments, using this control strategy and a similar catalytic artificial muscle, we obtained actuation frequencies in the order of 1 to 2 Hz (see text S3). Consistently, in this case, a main control objective is to design a tunable MCM that enables a stable oscillation of the surface temperature and, therefore, of the output strain produced by the artificial muscle.

Design of RoBeetle

To demonstrate the capabilities of the proposed 2H NiTi-Pt–based actuators, we built the autonomous RoBeetle prototype in Fig. 3A and Movie 1. This robot crawls by using a variable friction–based mode of locomotion. The proposed actuation approach, however, can be used to power a wide gamut of microrobotic platforms that locomote by walking (*13*), jumping (*36*), swimming (*37*), and flying (*38*). The combined mechanism for actuation, sensing, and feedback control is depicted in Fig. 3B; the integration of all the components of the robot required for autonomous operation—including the NiTi-Pt composite wire, MCM, fuel tank, and structural elements—is shown in the exploded view of Fig. 3 (C to H).

As seen in Fig. 3B, during the assembly process, one end of the NiTi-Pt composite wire is anchored to the fuel tank, and the other end, corresponding to the actuator output, is attached to a bias leaf spring required to maintain the SMA material under tension. Both a transmission and a sliding shutter are connected to this spring to be driven by the deformation of the NiTi-Pt wire. The locomotion pattern consists of a sequence of transitions between state 1 (upper illustration of Fig. 3B) and state 2 (bottom illustration of Fig. 3B). We used methanol as the fuel because it can be stored in liquid form and evaporates at an approximately constant rate at the atmospheric pressure. Accordingly, during state 1, the orifices of the sliding shutter remain aligned with those of the fuel tank, thus allowing methanol vapor to flow out from the container and reach the surface of the NiTi-Pt wire. As the catalytic surface is exposed to both fuel and oxygen, the SMA material contracts as illustrated in Fig. 2A, and the system transitions to state 2 as predicted by the plot in Fig. 2F, a period during which the tank valves remain closed. Sequentially, as the flow of fuel ceases, the SMA material expands, the shutter slides back to state 1, and the tank valves open to initiate a new actuation cycle.

Inspired by the control mechanism of the centrifugal governor (*21*), during the transitions from state 1 to state 2 and from state 2 to state 1, the slider shutter mechanism functions as a stabilizing controller for the catalytic reaction in a negative feedback loop. Namely, the supply of fuel decreases as the catalytic reaction accelerates because the tank valves steadily close as the shutter slides to state 2; conversely, the supply of fuel increases as the catalytic reaction decelerates because the tank valves steadily open as the shutter slides back to state 1. Note that from the control perspective, the areas of the tank and shutter orifices, the preset tension on the NiTi-Pt wire, and the stiffness of the leaf spring correspond to the parameters of the feedback controller that determines the performance and stability of the closed-loop system.

Although a rigorous mathematical analysis of the closed-loop dynamics of the system is beyond the scope of this paper, it is important to explain how the mechanical controller parameters must be selected to ensure functionality and stability. In this case, instability is equivalent to thermal runaway (*39*), a phenomenon characterized by a rapid increase of the surface temperature until the NiTi-Pt wire melts. The literature and experimental observations indicate that the rate of temperature variation depends monotonically on the flow rate of fuel, which, in this case, depends on the total area of the orifices of the tank and, coincidently, of the shutter. Specifically, if the fuel flow surpasses a critical point due to an excessive interface area between the tank and the catalytic surface, the closed-loop system becomes unstable. Furthermore, note that the preset tension of the wire and stiffness of the leaf spring also indirectly influence the flow rate of fuel and, therefore, the stability of the

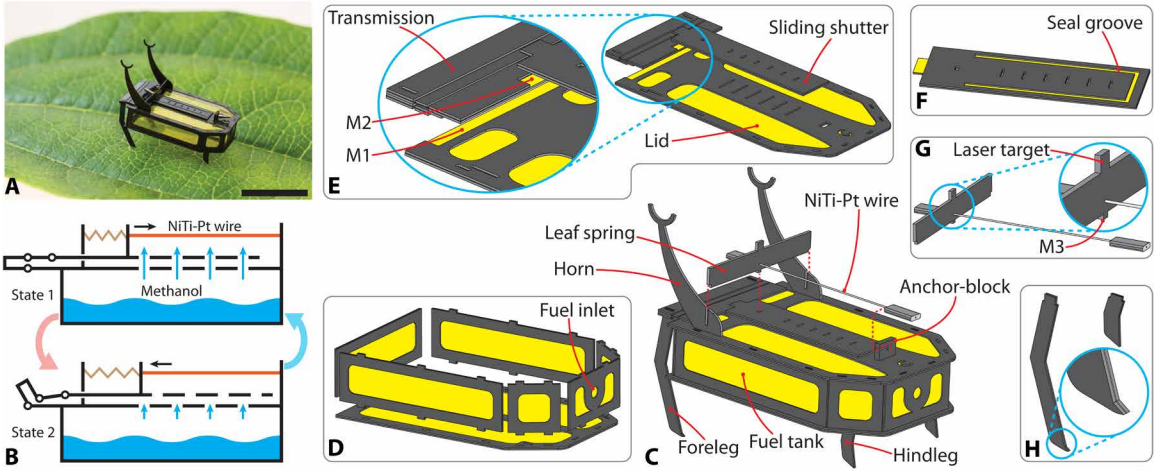

Fig. 3. Robotic design of the 88-mg insect-scale autonomous robot powered by fuel. (**A**) Photograph of a RoBeetle prototype resting on a leaf (the scale bar indicates a distance of 10 mm). (**B**) Schematic diagram of RoBeetle's actuation mechanism. (**C**) Exploded view of the robotic assembly. (**D**) Exploded view of the fuel tank subassembly. (**E**) Exploded view of the tank lid, transmission and sliding shutter. (**F**) Bottom side of the sliding shutter. (**G**) NiTi-Pt composite wire and leaf spring. (**H**) Forelegs and hindlegs with bioinspired backward-oriented claws.

Movie 1. RoBeetle, an 88-mg autonomous robotic insect powered by fuel. Summary of results and methods.

closed-loop dynamics. On the other hand, if the interface area between the tank and the catalytic surface is not sufficiently large for the flow of fuel to initiate and sustain catalytic combustion, the correct functionality of the actuation mechanism becomes infeasible. In this case, through an experimental tuning process, we enabled the actuation mechanism to self-oscillate stably and robustly while driving the locomotion of the RoBeetle prototype.

As seen in Fig. 3 (B and C), the actuation output is transformed into a rotational motion using a four-bar transmission inspired by the flight muscles of dipteran insects (*6*, *40*, *41*) and that can be modeled as a static mapping (*41*, *42*). As illustrated in Fig. 3 (B, C, and E), the rotational motion produced by the transmission is transformed into locomotion through two joint active forelegs and two fixed hindlegs, which use anisotropic friction to sequentially slide forward and anchor to the ground. Specifically, during the transition from state 1 to state 2, the pair of hindlegs anchors the robot to the ground, whereas the pair of forelegs rotates clockwise and slides forward; similarly, during the transition from state 2 to state 1, the pair of forelegs rotates counterclockwise while anchored to the ground and the pair of hindlegs slides forward.

Now, we describe the components of the robot and the assembly process in Fig. 3 (C to H); the details regarding fabrication are presented in Materials and Methods. On the basis of their functionality, the components are grouped into four categories.

1) The first category includes the parts that compose the torso of the robot, which is also the fuel tank that stores the methanol (Fig. 3, C and D). The bottom and sides of the tank are built from seven pieces made of carbon fiber–polyimide composites that are assembled together using tab-and-slot features. Cyanoacrylate (CA) glue is applied on all the clearances to seal the tank and make it liquid tight.

2) The second category is formed by the components of the MCM: the tank lid and sliding shutter (Fig. 3E). These parts are assembled together with the transmission during a step executed before the final assembly. As shown in the detailed view of Fig. 3E, the mating fixture M1 on the lid is attached to the grounded link of the transmission using CA glue; then, the shutter is glued to the slider input link of the transmission at the mating fixture M2. To create the interface between the container and the NiTi-Pt wire, a row of six 0.1 mm–by–1.5 mm rectangular orifices, placed at regular intervals of 1 mm, is perforated on the tank lid; correspondingly, six 0.1 mm–by–0.5 mm rectangular apertures are perforated on the shutter according to the same pattern. These interacting matching perforations function as synchronized microvalves, which are used to control the flow of fuel that feeds the catalytic reaction on the surface of the NiTi-Pt wire. Because the flow rates depend monotonically on the overlapped areas of the valve mechanism, the shape and configuration of the matching perforations determine the heating and cooling profiles of the SMA material. During the design process, by performing a series of tethered tests, using robotic prototypes with a variety of sliding valve configurations, we identified the parameters for an MCM that enables the NiTi-Pt–based artificial muscle that drives the RoBeetle prototype to operate within desired temperature ranges. We performed an evaporation experiment to measure the fuel flow rates for the robotic design (text S4 and movie S1), and the experimental results were used to calibrate an analytical model that describes the diffusion process of the methanol vapor (text S5). To prevent leakage, seal grease is applied to the groove carved on the bottom of the sliding shutter, as shown in Fig. 3F. Last, the complete MCM is used to cap the tank, thus forming the torso of the microrobot as shown in Fig. 3C.

3) The third category is composed of the parts that constitute the actuation mechanism, including the NiTi-Pt wire, the transmission (Fig. 3E), the leaf spring (Fig. 3, C and G), two horn-shaped static

arms that are used to mount the leaf spring, and the back anchor-block fixture that holds the composite wire (Fig. 3C). The three mounting pieces are connected to the tank lid using socket-lock mechanisms and permanently fixed using CA glue. The leaf spring is a stiff bar made from carbon fiber with an orifice through which the NiTi-Pt wire was threaded (Fig. 3G). The two ends of the wire are crimp-clamped to install it on the robot and set its tension. The piece composed by the spring and the crimp-clamped wire is attached to the torso of the robot by first inserting the rightmost end of the wire into the slot of the anchor block, as indicated by the red dashed line; then, the bottom locking protrusion M3 (see Fig. 3G) and both sides of the spring are inserted into the mating orifice carved on the shutter and the slots of the horns, respectively. This configuration enables the artificial muscle to simultaneously drive the sliding shutter and the transmission through the leaf spring. In agreement with the thermomechanical description in Fig. 2 (B and F), the SMA wire must be preloaded to function effectively as an actuator; for this reason, the initial condition of the system is set with the leaf spring bent and the wire in tension. This initial state is enforced by simply using a NiTi-Pt wire with an unexcited length that is smaller than the distance between the slots of the horns and the anchor block, namely, 9.8 mm at 25°C instead of 9.88 mm. For the robot used in the locomotion experiments, the measured spring stiffness is ~4.26 N/mm (see text S6) with a corresponding loading stress of ~168 MPa. Note that the proposed robotic design allows us to freely set the loading stress acting on the NiTi-Pt wire by adjusting the location of the crimp clamps. Similarly, the entire artificial muscle can be easily replaced if different geometrical or catalytic characteristics for effective operation are required.

4) The last category is composed of the bioinspired microrobotic legs with claws that are capable of inducing anisotropic friction, thus emulating the friction mechanism used by beetles of the subspecies *Pachnoda marginata peregrina* (*43*). As seen in Fig. 3 (C and H), the two forelegs are installed at the distal end of the transmission and the two hindlegs at the bottom of the tank, using tab-and-slot features. The overall design and limb configuration enable RoBeetle prototypes to locomote unidirectionally using the simple proposed two-anchor crawl gait, which is similar to the mode observed in some types of inchworms, for example, the patterns of caterpillars of the species *Manduca sexta* (*44*), which conceptually also resemble the locomotion method used by the soft robot in (*45*). All the fundamental parameters of the RoBeetle prototype used in the experiments are summarized in table S3.

Tethered stationary experiments

To obtain adequate parameters for the design of the MCM, we conducted a series of tethered experiments using several RoBeetle prototypes. Specifically, we measured the most relevant variables associated with the operation of the microrobot, including the surface temperature of the NiTi-Pt wire and the resulting self-oscillatory actuation strain, as shown in Fig. 4 and movie S2. Because of limitations in miniaturization, installation, and signal transmission, the use of onboard wireless sensors to accurately measure temperature and strain in a moving subgram robotic insect is still extremely challenging, which justifies the stationary experimental approach depicted in Fig. 4A. During these tests, one hindleg of the robot is held in place using a pair of cross-lock tweezers, whereas the other three legs are left to freely dangle in the air; the deformation of the NiTi-Pt wire is measured with a laser displacement sensor (Keyence LK-031) that is installed in front of the robot so that the emitted laser beam hit the target area of the leaf spring shown in Fig. 3G. To measure (to indirectly observe) the temperature of the catalytic reaction, a Pt-black–coated thermocouple (type K, Omega CHAL-002) is installed next to the NiTi-Pt wire. Note that this thermocouple measures the temperature close to a single point of the catalytic surface and that thermocouples exhibit dynamics that delay and filter the high-frequency content of the true signals. Therefore, the signal obtained as shown in Fig. 4A is a reasonable estimation but not the true temperature of the SMA material. Further details regarding the experimental setup are presented in text S7.

Measured temperature and strain signals corresponding to a representative stationary experiment, obtained using the prototype in Fig. 3A, are shown in Fig. 4B. From this plot, it can be deduced that the temperature of the catalytic reaction was mechanically controlled to continually oscillate within the desired range; accordingly, the artificial muscle produced effective periodical strain outputs. These results, therefore, demonstrate that the robot is able to operate autonomously when controlled by the proposed MCM. In this case, the measured temperature is composed of a main oscillatory signal and a set of components with higher frequencies that resemble random patterns.

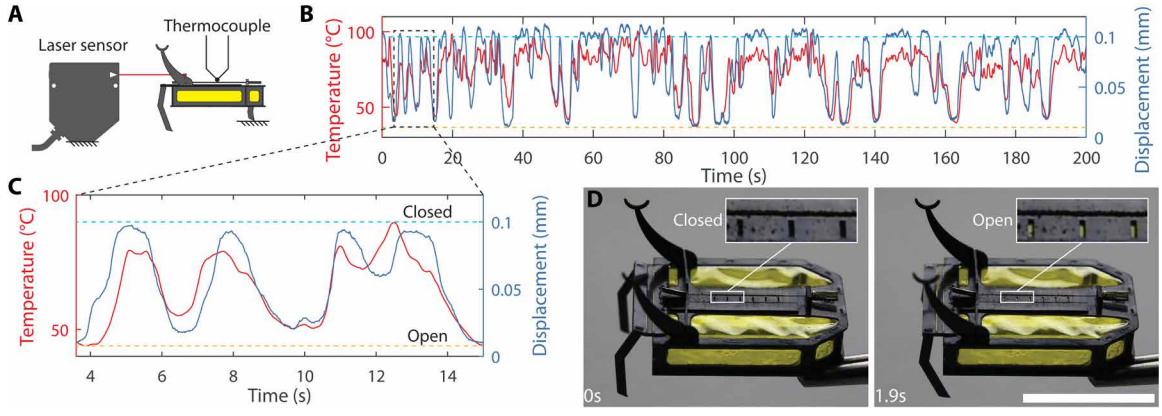

Fig. 4. Tethered stationary experiments used to characterize the RoBeetle prototype. (**A**) Schematic diagram of the experimental setup (not to scale). (**B** and **C**) Temperature and displacement responses generated by the NiTi-Pt composite artificial muscle during operation and associated zoomed-in view. The top and bottom dashed lines indicate the closed and open positions of the sliding shutter mechanism, respectively. (**D**) State 2 (closed valves) and state 1 (open valves) of the actuation cycle (1.9 s, from state 2 to state 1). The insets show the closed and open states of the sliding shutter mechanism (the scale bar indicates a distance of 10 mm).

Despite the disturbances affecting the system, the principal oscillatory component remains bounded within the range from 37° to 100°C and is sufficiently regular to enable locomotion. Disturbances appear because the diffusion process of methanol vapor from the orifices of the sliding shutter to the surface of the NiTi-Pt wire and the catalytic reaction can be easily affected by gusts of air. These issues can be solved by adding a protecting fixture to the design to make the artificial muscle windproof. As seen in Fig. 4C, the general trend of the strain output is to approximately follow the measured temperature signal; this behavior is consistent with the hysteretic model in Fig. 2 (B and F).

We hypothesize that the observed discrepancies between the evolutions of the two signals in Fig. 4C and the identified relationship in Fig. 2F reflect inaccuracies associated with the method used to measure temperature. This issue is explained because, as illustrated in Fig. 4A, a small (0.0508 mm in diameter) thermocouple's bead is placed right next to the surface of the NiTi-Pt wire, and not wrapped around its cross section, to avoid mechanical interferences with the actuation cycle. In addition to obtaining measurements as shown in Fig. 4A, to heuristically evaluate the entire functionality of the system, we also took an infrared thermal video of a representative tethered experiment (movie S3). Using the thermodynamic model of the artificial muscle in text S8 and data obtained through the tethered experiments in Fig. 4, we estimate that the actual overall thermal efficiency of the NiTi-Pt–based actuator used by a RoBeetle prototype during operation has an average value of about 16%. This value comprises both fuel utilization and the heat transfer efficiency associated with the NiTi-Pt composite wire. By considering an efficiency of 3% for the conversion of heat into mechanical work, performed by the NiTi material (*31*), we estimate that the overall energy efficiency of a RoBeetle prototype is approximately 0.48%. We believe that this heat transfer efficiency can be improved by reducing the thickness of the layer of Pt; the fuel utilization efficiency can be improved by installing multiple NiTi-Pt composite wires over the sliding shutter to capture more fuel vapor for combustion. Despite the seemingly low overall efficiency (0.48%) of the proposed catalytic artificial muscle, this actuator exhibits a superior performance in providing energy for autonomy compared to battery-powered schemes due to the utilization of HED fuels (see text S9).

Autonomous locomotion

To validate the proposed actuation approach and study the untethered locomotion performance of the RoBeetle prototype, we performed two types of experiments: autonomous crawling inside a

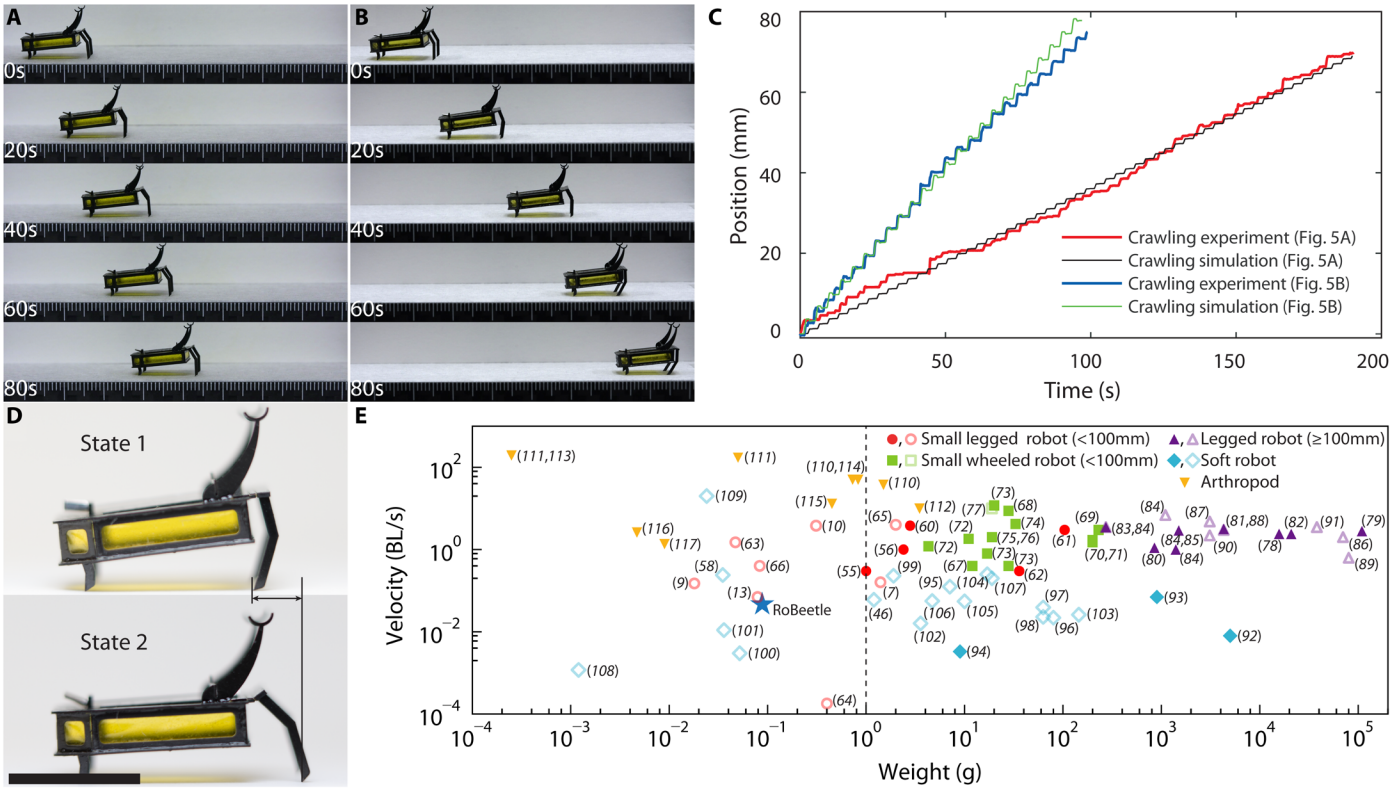

Fig. 5. Autonomous locomotion under two atmospheric conditions. (**A**) Photographic sequence of autonomous crawling on a flat surface inside a stationary undisturbed atmosphere. (**B**) Photographic sequence of autonomous crawling inside a gently moving atmosphere. (**C**) Positions of the robot during the locomotion experiments in (A) and (B); both experimental signals are compared to simulation results obtained with the dynamic model in text S11. (**D**) Two states in a locomotion cycle. At state 1, the hindlegs of RoBeetle anchor and the forelegs start to slide forward as the artificial muscle contracts due to the opening of the sliding shutter. At state 2, the forelegs anchor to the ground using claws, and the hindlegs slide forward as the artificial muscle extends. The scale bar indicates a distance of 10 mm. (**E**) Locomotion velocities of various robots and arthropods in BL per second versus body weight in grams. The solid symbols correspond to robots that are autonomous, whereas robots relying on external power sources are represented with hollow symbols. See table S4 for detailed data. The robots are indicated using their corresponding reference numbers. The location of RoBeetle is marked with a blue star.

stationary atmosphere and autonomous crawling inside a gently moving atmosphere. These two experiments are intended to highlight the worst-case and best-case conditions of operation based on the average crawling velocity. An instance of the first type of locomotion test is shown in Fig. 5A; an instance of the second type of locomotion test is shown in Fig. 5B. The complete set of experiments is shown in movie S4. From this movie, relevant locomotion data were extracted and processed using object tracking software (see Materials and Methods). The positions of the robot as functions of time, corresponding to both tests in Fig. 5 (A and B), are shown in Fig. 5C. The resulting experimental gait resembles the two-anchor crawl locomotion mode used by inchworms (*46*); during operation, the distance from the claws of the hindlegs to the claws of the forelegs cyclically increases, as the artificial muscle contracts, and decreases, as the artificial muscle extends (see Fig. 5D).

A distinguishing characteristic of the locomotion mechanism used by RoBeetle, with respect to that used by inchworms, is the utilization of anisotropic friction. Specifically, as shown in Fig. 3H, the backward-oriented claws of the four legs generate frictions with different magnitudes depending on the direction of the sliding motion. Here, to explain this notion, we use an extremely simplified quasi-static model given by

$$\begin{aligned} f_{\mathrm{f}}^{+} &= \mu_{\mathrm{f}}^{+} N_{\mathrm{l}} \ll \mu_{\mathrm{f}}^{-} N_{\mathrm{l}} = f_{\mathrm{f}}^{-} \\ f_{\mathrm{h}}^{+} &= \mu_{\mathrm{h}}^{+} N_{\mathrm{l}} \ll \mu_{\mathrm{h}}^{-} N_{\mathrm{l}} = f_{\mathrm{h}}^{-} \\ \mu_{\mathrm{f}}^{+} &= \mu_{\mathrm{h}}^{+} \\ \mu_{\mathrm{f}}^{-} &= \mu_{\mathrm{h}}^{-} \end{aligned} \tag{1}$$

where, assuming a perfectly balanced distribution of the robot's weight, N_{l} represents the normal force exerted on each leg; f_{f}^{+} is the magnitude of the friction force that opposes the forward sliding motion of each of the two forelegs when the system is transitioning from state 1 to state 2 (Fig. 5D); f_{f}^{-} is the magnitude of the friction force that opposes the backward sliding motion of each of the two forelegs when the system is transitioning from state 2 to state 1; correspondingly, μ_{f}^{+} and μ_{f}^{-} are positive friction coefficients satisfying $\mu_{\mathrm{f}}^{+} \ll \mu_{\mathrm{f}}^{-}$; f_{h}^{+} is the magnitude of the friction force that opposes the forward sliding motion of each of the two hindlegs when the system is transitioning from state 2 to state 1; f_{h}^{-} is the magnitude of the friction force that opposes the backward sliding motion of each of the two hindlegs when the system is transitioning from state 1 to state 2; and, correspondingly, μ_{h}^{+} and μ_{h}^{-} are positive friction coefficients satisfying $\mu_{\mathrm{h}}^{+} \ll \mu_{\mathrm{h}}^{-}$. In agreement with experimental observations and the model specified by Eq. 1, the body of the robot remains immobile during the transition from state 1 to state 2 because $\mu_{\mathrm{f}}^{+} \ll \mu_{\mathrm{h}}^{-}$. On the other hand, the body moves forward during the transition from state 2 to state 1 because $\mu_{\mathrm{h}}^{+} \ll \mu_{\mathrm{f}}^{-}$. Considering that obtaining kinetic descriptions of friction for the tiny legs of the prototype is a nontrivial experimental task, in texts S10 and S11 (Part II), we present a method to indirectly measure coefficients for quasi-static friction models. These measurements validate the anisotropic characteristic of the friction forces induced by the interaction of the legs of the robot with the ground, as intended by design; however, they also show that the model in Eq. 1 lacks the sophistication required to make quantitative predictions. To remedy this issue, in text S11, we present an input-output dynamic model of the locomotion gait that can be used to implement high-fidelity numerical simulations.

The experiments in Fig. 5 (A and B) were recorded while the RoBeetle prototype crawled on a perfectly horizontal flat plane covered with smooth paper tissue. This surface is homogenous with a moderate roughness R_a = 7.528 μm, which makes it suitable for studying the crawling of the robot under two different conditions of operation. In the first test, the robot crawls autonomously inside a static atmosphere so that the surface of the NiTi-Pt wire passively cools down during the actuation cycle, mostly due to heat conduction; the performance achieved under this condition is the expected worst case. In the second test, the robot crawls autonomously inside a gently moving atmosphere so that the surface of the NiTi-Pt wire passively cools down during the actuation cycle, due to both conduction and convection; however, experimental observations suggest that the most relevant effect of airflow on the catalytic surface of the NiTi-Pt composite wire is the removal of residual methanol when the sliding shutter is closed (state 2 in Fig. 3B), which completely stops the surface chemical reactions. Overall, the performance achieved under the second atmospheric condition is expected to be better than that achieved in the first case due to the combined effects of convection and the periodic removal of residual fuel vapor and heat from the surface of the composite wire. In the particular case shown in Fig. 5 (B and C), we accelerate the airflow field surrounding the robot by simply waving a paper card with dimensions 7.62 cm by 12.7 cm at a distance of ~10 cm over the prototype.

As seen Fig. 5C, in the test in Fig. 5A, the robot crawls in small steps with a corresponding mean stride of ~1.2 mm. The irregularities observed in the crawling pattern are caused by disturbances affecting the diffusion process of methanol vapor, which is consistent with the results obtained through the tethered stationary experiments described in Fig. 4. In contrast, in the test in Fig. 5B, the robot exhibits a regular crawling pattern with a corresponding mean stride of ~2.83 mm. This improved operational regularity is expected to be produced, at least in part, by the faster cooling rate during each actuation cycle. Notably, however, the measured average actuation period of the second experiment is longer than that of the first—namely, 3.7 and 3.3 s, respectively. This observation indicates that during the performance of the second experiment, the SMA wire operates according to wider hysteretic minor loops than those corresponding to the first experiment. Consequently, the better performance achieved by the robot during the second experiment is the result of a larger actuation amplitude and not a faster frequency. We hypothesize that this phenomenon is the result of not only faster cooling, but also of faster heating. This conclusion follows from noticing that if the forelegs fully return to state 1, the sliding shutter opens entirely and, therefore, the condition of maximum fuel supply is reached. Directly from the data in Fig. 5C, we estimate that the robot's average locomotion velocity during the experiment in Fig. 5A is ~0.37 mm/s and that the robot's average locomotion velocity during the experiment in Fig. 5B is ~0.76 mm/s.

Simulation results obtained using the dynamical description of the friction-based crawling mechanism presented in text S11 are also plotted in Fig. 5C. Specifically, we model locomotion as a mapping for which the input is the displacement output generated by the artificial muscle (equivalent to the angle θ defined in text S11 and fig. S7) and the output is the position of the robot along a straight line (see Fig. 5, A and B). Consistently, considering the hysteretic dynamics of SMA actuators (see Fig. 2B), the input to the crawling

mechanism is modeled as a sequence of identical one-period bell-shaped signals, as defined in text S11 and depicted in fig. S7; the signal parameters (shown in table S7) were identified from the data obtained through the tethered and untethered experiments already described above. From the comparisons in Fig. 5C, we deduce that the model captures the main features of the crawling process; namely, the mean locomotion speeds match almost perfectly and the distinct staircase increments in position produced by the two-anchor crawling are approximately replicated. The observed slight discrepancies between the simulated and experimental signals are explained by inhomogeneities in the locomotion path and disturbances affecting the diffusion of fuel vapor from the valves to the catalytic surface of the wire. Note that because of the regularity of actuation created by the enhancing effect of the removal of residual fuel from the surface of the NiTi-Pt composite wire, for the test in Fig. 5B, the simulated model generates a position signal that matches even some of the smallest features of the measurement. For example, the simulation replicates the slight backward motion of the robot that is produced by micrometric sliding displacements of the hindlegs during the transition from state 1 to state 2; a phenomenon that, as seen in movie S4 and Fig. 5C, is most evident during crawling between times 50 and 80 s.

The performance of RoBeetle, compared to those of various arthropods and the set of most advanced terrestrial locomoting robots, is shown in Fig. 5E. Here, the horizontal axis indicates weight in a $\log_{10}$ scale and the vertical axis indicates the normalized velocities of the compared systems. The velocities are normalized to be expressed in the same units; namely, body lengths per second (BL/s). We considered five classes of systems: arthropods (yellow triangles); soft robots (blue diamonds); normal-sized legged robots (purple triangles), characterized by lengths equal or larger than 100 mm; small wheeled robots (green squares), characterized by lengths smaller than 100 mm; and small legged robots (red circles), characterized by lengths smaller than 100 mm. In this classification, autonomous robots are indicated with solid symbols and tethered robots using hollow symbols; the performance of the RoBeetle prototype is indicated with a blue star. Note that RoBeetle is one of the lightest subgram insect-sized autonomous robots created to date; also, RoBeetle is the fastest autonomous crawling robot relative to its size (BL < 20 mm) that is capable of operating for more than a few seconds.

Functional capabilities and locomotion performance

From the most basic navigational standpoint, an autonomous terrestrial robot must be capable of climbing inclines, carrying payloads, and locomoting on various different surfaces. Thus, to assess the functionality of RoBeetle, we performed several further experiments. The first is ramp climbing, shown in Fig. 6 (A to C). In this case, we used a tilted glass slide with a surface area of 5.08 cm by 7.62 cm covered with a smooth piece of paper tissue as the inclined plane to be climbed by the robot. Figure 6 (A to C) shows the robot crawling on inclines with slopes of 5°, 10° and 15°, respectively. The prototype can easily climb the ramps with slopes of 5° and 10° and stalls while climbing the ramp with a slope of 15°; the corresponding measured velocities, compared to that of the horizontal case, are shown in Fig. 6D. The complete set of experiments is shown in

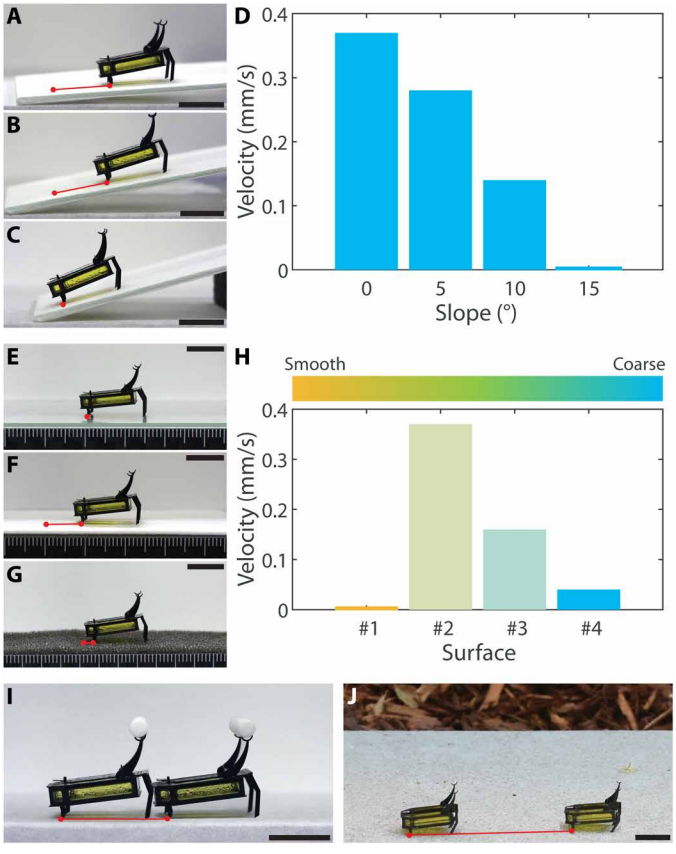

Fig. 6. Locomotion under different conditions and achieved mean velocities. (**A** to **C**) The RoBeetle prototype climbs on inclined planes with slopes of 5°, 10° and 15°, respectively. The red lines indicate the displacements from the initial to the final positions reached in 45, 85 and 45 s, respectively. The scale bars indicate a distance of 10 mm. (**D**) Mean locomotion velocities versus angle of inclination. (**E** to **G**) The robot crawls on surfaces with different levels of roughness, namely, glass, pacopad (Pacothane Technologies, Winchester, MA), and polyurethane charcoal foam. The red line is the displacement from the initial to the final positions. The duration is 60 s, and the scale bars indicate a distance of 10 mm. (**H**) Mean locomotion velocities on four surfaces with different levels of roughness, numbered from 1 to 4, corresponding to glass, smooth paper tissue, pacopad and polyurethane charcoal foam. (**I**) Time-lapse image of the robot while crawling at 0.22 mm/s and carrying a 71-mg plastic stick on its horns. The duration is 80 s, and the scale bar indicates a distance of 10 mm. (**J**) Time lapse of the robot autonomously crawling outdoors on a concrete sideway. The mean velocity is 0.23 mm/s. The duration is 200 s and the scale bar indicates a distance of 10 mm.

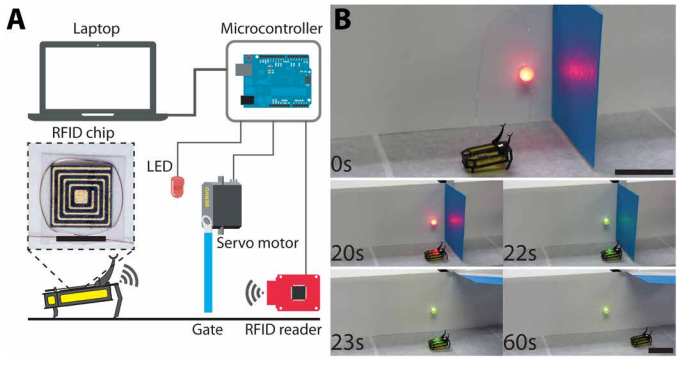

Fig. 7. Robot-environment interaction enabled by onboard RFID chip. (**A**) Diagram of the experimental setup. The scale bar inside the inset indicates a distance of 2 mm. (**B**) Photographic sequence of the experiment. The scale bars indicate a distance of 20 mm.

movie S5. In these tests, the crawling velocity decreases monotonically as the value of the slope increases. This phenomenon is explained by a decrease of the normal forces exerted by the inclined plane under the legs of the robot; as a result, the corresponding total friction acting on the robot is reduced and there exists a critical slope for which crawling becomes infeasible. The effects of the inclined path on the volume distribution of the liquid methanol are negligible because the viscosity and surface tension can hold the thin layer of fuel (~0.2 mm) approximately parallel to the tank lid (see movie S5).

In a second set of experiments, we tested the crawling capabilities of the robot on surfaces with different levels of roughness R_a—specifically, smooth glass with R_a = 0.009 μm (Fig. 6E), the already described piece of paper tissue with R_a = 7.528 μm (Fig. 5A), pacopad with R_a = 10.419 μm (Fig. 6F) and polyurethane charcoal foam with R_a = 17.922 μm (Fig. 6G). The resulting velocities for these cases are shown in Fig. 6H, correspondingly labeled as #1, #2, #3, and #4; with the current claw design, the robot achieved the fastest velocity on surface #2. Details are presented in text S12 and movie S6. In a third set of experiments (Fig. 6I), the robot carried on its horns a 71-mg cylindrical weight while crawling at a speed of 0.22 mm/s. Similar tests demonstrated that the robot can carry a maximum payload of 230 mg (~2.61× the prototype's weight). These experiments are shown in movie S7. Last, as shown in Fig. 6J, to demonstrate RoBeetle's ability to locomote outdoors and its potential for real-world applications, we placed a prototype on a concrete sideway. Under this condition, the robot was able to operate autonomously as it carried onboard both its own power source (fuel) and MCM (see movie S8). This experimental demonstration provides evidence of the feasibility of creating fully autonomous subgram insect-scale robots capable of operating in nonlaboratory environments.

Demonstration of RoBeetle carrying payloads

In previous sections, we demonstrated the basic capabilities of RoBeetle and discussed the observed performance during locomotion. In this section, we demonstrate how the capacity of RoBeetle to carry payloads enables environment-robot interactions that are usable to perform simple automated tasks. Specifically, we installed a writable 6-mg radio-frequency identification (RFID) chip and a booster antenna on the robot, as shown in Fig. 7A, to enable simple interactions with the environment. Generally speaking, an RFID chip is a sensor that works independently to collect, store and transmit data—its own position, for example (*47*). In the experimental example in Fig. 7 and movie S9, a RoBeetle prototype crawls along a straight path toward a dummy gate driven by a servomotor, while the onboard RFID chip stores the opening code. Thus, when the robot enters the range of the RFID reader, located 50 mm behind the gate, the code broadcasted by the onboard transmitter is detected (at time 20 s in Fig. 7B); then, a microcontroller identifies the code and switches the state of a light-emitting diode (LED) indicator from red to green (at time 22 s in Fig. 7B). Last, the microcontroller sends a command to the servomotor to lift the gate, thus allowing the robot to pass through (23 to 60 s in Fig. 7B). Further details are discussed in text S13.

DISCUSSION

We presented RoBeetle, a subgram insect-scale robot capable of crawling autonomously and performing simple tasks. This accomplishment was made possible by the physical realization and combination of two technological concepts: a controllable artificial muscle driven by flameless catalytic combustion and an integrated preprogrammable millimeter-scale MCM. Accordingly, the robot is built as an integrated system in which the actuator, sensor used for feedback, and MCM constitute a compact functional unit. Our approach enabled the development of artificial muscles that have both the HWDs of SMA actuators and the ability to use HED fuels (2H).

Presently, the speed of actuation is mainly limited by the diffusion rate of fuel and bandwidths of the SMA wires. Therefore, to amplify the frequencies of the actuator outputs, we can simply increase the speed of fuel delivery by using liquefied fuels, stored in pressurized containers, such as butane or propane. Furthermore, as suggested in a recent study (*48*), the bandwidth of SMA-based actuators can be substantially widen (up to 35 Hz) by adopting unconventional mechanical configurations of thin SMA wires (38.1 μm in diameter). In particular, the magnitude of the mechanical output and efficiency of the proposed actuation method can be significantly improved by arranging multiple fiber-like thin artificial muscles in hierarchical configurations similar to those observed in sarcomere-based animal muscle. In addition, the integrated mechanical controller that uses the strain actuator output as feedback was validated and demonstrated to enable the autonomous electronics-free operation of the tested RoBeetle prototype.

In summary, RoBeetle is a biologically inspired system whose fuel-powered design may serve as a model for the creation of a new diverse generation of autonomous microrobots capable of terrestrial, aquatic, and aerial locomotion.

MATERIALS AND METHODS

Fabrication of NiTi-Pt composite wires

A NiTi-Pt composite wire is fabricated by coating a thin rough layer of Pt, which acts as a catalyst for the flameless combustion of fuel, on the surface of an SMA wire with a diameter of 50.8 μm. In this case, the thermally excitable SMA material is Nitinol, a $Ni_{50\%}Ti_{50\%}$ compound produced by Dynalloy with a nominal transition temperature of 90°C. The obtained homogeneity of thickness and structural integrity of the resulting catalyst layers, which are of critical importance to achieve reliable, repeatable, and controllable catalytic reactions, are one of the key elements that made possible the fabrication of a high-quality and mechanically robust NiTi-Pt composite wire and its integration into the chassis of a RoBeetle prototype. As depicted in fig. S1 (A to K), the first step in the fabrication process is to crimp the NiTi wire at two locations with compressible tubes (McMaster-Carr 89875K85 with an outer diameter of 0.635 mm and a wall thickness of 0.152 mm) using a 10-ton handheld hydraulic crimping tool. Then, the tubes are cut to have a length of 2 mm using a flush cutter. The resulting interior length of the crimped NiTi wire is exactly 9.8 mm, a length that is precisely ensured by using a fixture tool (fig. S1, D and E).

As shown in fig. S1H, the second step in the fabrication procedure is the application of a uniform layer of thermally conductive paste (Omega OT-201), which acts as a permanently wet adhesive on the surface of the NiTi wire. To ensure micrometric precision, the paste is applied using a microbrush under an optical microscope; the resulting layer of conductive paste has an average thickness of 0.6 μm and remains uncured at room temperature (see fig. S1H). Last, the outer layer of Pt catalyst is added to the piece of SMA material to finalize the fabrication of the NiTi-Pt composite wire,

by simply immersing it into a heap of Pt powder (Pt-black HiSPEC 1000, Alfa Aesar), as shown in fig. S1I. This process is repeated until the desired shapes and configurations of the 3D structures that composed the catalyst layer are achieved (see fig. S1K); during fabrication, the quality of the coating is controlled by continually monitoring its condition under a microscope. The finished NiTi-Pt composite wires have outer diameters of 87 μm. All the micrometer-scale images in the paper were captured using the same SEM (JEOL JSM-7001f-SEM).

The fixture tool used to enforce the precise length of the wire (fig. S1, D and E) has dimensions of 9.8 mm by 2 mm by 2.36 mm and simply consists of three pieces made from a 185-μm-thick carbon fiber–polyimide composite sheet, assembled in a 3D configuration. A diode-pumped solid-state (DPSS) laser (DCH-355-3, Photonics Industries) with a focused beam diameter of 10 μm was used to cut out, from the composite sheet, the pieces composing the centimeter-scale structure; then, these parts were joint together manually by matching premachined tab-and-slot assembly features.

Note that the microfabrication procedure presented in this section is the result of an intense and exhaustive research process and, once perfected, has exhibited an experimental yield close to 100%. The resulting NiTi-Pt composite wires are mechanically robust and can function reliably for hours without the issues reported in (*49*, *50*).

Fabrication of the robotic prototypes

With the exception of the artificial muscles, all the mechanisms and structural components of the RoBeetle prototypes were designed and are fabricated using the SCM method, especially some of the techniques described in (*51*). In specific, the fuel tank, lid, legs, sliding shutter and horns of the prototype shown Fig. 3A were made from 185-μm-thick composite laminates composed of two 80-μm-thick carbon fiber layers (top and bottom) and one central 7.5-μm-thick polyimide film layer (Kapton HN 30 gauge, DuPont); the transmission and anchor block were made from 380-μm-thick laminates fabricated by bonding two 185-μm-thick layers together using a 12.5-μm-thick adhesive film (Pyralux FR1500, DuPont); and the leaf spring was made from a 190-μm-thick carbon fiber laminate. In this case, following the SCM method, all the 3D microparts were created by assembling and folding featured two-dimensional (2D) components that were cut from the composite sheets using the DPSS laser. In general, during 3D assembly, the 2D parts are connected to each other by matching tab-and-slot features; then, the connections and corners are rigidized and strengthen using CA glue (Loctite 416, Henkel). To gas-tight seal the interface between the tank lid and sliding shutter, a thin layer of grease (Parker O-ring lubricant) is applied to the 80-μm-deep seal groove described in Fig. 3F.

Locomotion experiments

Several crawling experiments were performed on different surfaces as described in Results. The primary locomotion path, which was used in the experiments of Fig. 5, was built by tightly wrapping a 3-mm-thick acrylic sheet with laboratory tissue (Kimtech 34155CT Kimwipes). The acrylic platform serves as a rigid and even base, and the smooth paper tissue provides a surface with the adequate roughness for sustained locomotion. In the performance of each crawling experiment, 20 μl (15.8 mg) of methanol were injected into the tank of the robot; then, the prototype in the configuration corresponding to state 1 (Fig. 5D) was placed on the locomotion path using a pair of tweezers. As seen in Fig. 5 (A and B), a metric ruler was used to indicate the scale of the robot in relation to the path. All the indoor tests were carried out at about 25°C and 48% relative humidity. All the movies were recorded with a digital single-lens reflex camera (Nikon D7200) at 30 frames per second. Basic postprocessing of the videos, such as clipping from the raw footages and exportation, was done using the iMovie Apple application. To extract locomotion data for analysis, the exported videos were processed using Open Source Computer Vision (OpenCV). The estimated positions over time corresponding to the two main experiments discussed in this paper are shown in Fig. 5C.

SUPPLEMENTARY MATERIALS

robotics.sciencemag.org/cgi/content/full/5/45/eaba0015/DC1

REFERENCES AND NOTES

1. G.-Z. Yang, J. G. Bellingham, P. E. Dupont, P. Fischer, L. Floridi, R. J. Full, N. Jacobstein, V. Kumar, M. McNutt, R. Merrifield, B. J. Nelson, B. Scassellati, M. Taddeo, R. H. Taylor, M. M. Veloso, Z. L. Wang, R. J. Wood, The grand challenges of *Science Robotics*. *Sci. Robot.* **3**, eaar7650 (2018).
2. R. St. Pierre, S. Bergbreiter, Toward autonomy in sub-gram terrestrial robots. *Ann. Rev. Control Robot. Auton. Syst.* **2**, 231–252 (2019).
3. K. Y. Ma, P. Chirarattananon, S. B. Fuller, R. J. Wood, Controlled flight of a biologically inspired, insect-scale robot. *Science* **340**, 603–607 (2013).

4. S. B. Fuller, Four wings: An insect-sized aerial robot with steering ability and payload capacity for autonomy. *IEEE Robot. Autom. Lett.* **4**, 570–577 (2019).
5. X. Yang, Y. Chen, L. Chang, A. A. Calderón, N. O. Pérez-Arancibia, Bee$^+$: A 95-mg four-winged insect-scale flying robot driven by twinned unimorph actuators. *IEEE Robot. Autom. Lett.* **4**, 4270–4277 (2019).
6. R. J. Wood, Design, fabrication, and analysis of a 3DOF, 3cm flapping-wing MAV, in *Proceedings of the 2007 IEEE/RSJ International Conference on Intelligent Robots and Systems (IROS)*, San Diego, CA, 29 October to 2 November 2007 (IEEE, 2007), pp. 1576–1581.
7. D. Lee, S. Kim, Y.-L. Park, R. J. Wood, Design of centimeter-scale inchworm robots with bidirectional claws, in *Proceedings of the 2011 IEEE International Conference on Robotics and Automation (ICRA)* (IEEE, 2011), pp. 3197–3204.
8. Y. Bar-Cohen, *Electroactive Polymer (EAP) Actuators as Artificial Muscles: Reality, Potential, and Challenges* (SPIE Press, Bellingham, WA, 2004), vol. 136.
9. D. S. Contreras, D. S. Drew, K. S. J. Pister, First steps of a millimeter-scale walking silicon robot, in *Proceedings of the 2017 19th International Conference on Solid-State Sensors, Actuators and Microsystems (TRANSDUCERS)* (IEEE, 2017), pp. 910–913.
10. S. Miyashita, S. Guitron, M. Ludersdorfer, C. R. Sung, D. Rus, An untethered miniature origami robot that self-folds, walks, swims, and degrades, in *Proceedings of the 2015 IEEE International Conference on Robotics and Automation (ICRA)*, Seattle, WA, 26 to 30 May 2015 (IEEE, 2015), pp. 1490–1496.
11. W. Hu, G. Z. Lum, M. Mastrangeli, M. Sitti, Small-scale soft-bodied robot with multimodal locomotion. *Nature* **554**, 81–85 (2018).
12. S.-J. Park, M. Gazzola, K. S. Park, S. Park, V. Di Santo, E. L. Blevins, J. U. Lind, P. H. Campbell, S. Dauth, A. K. Capulli, F. S. Pasqualini, S. Ahn, A. Cho, H. Yuan, B. M. Maoz, R. Vijaykumar, J.-W. Choi, K. Deisseroth, G. V. Lauder, L. Mahadevan, K. K. Parker, Phototactic guidance of a tissue-engineered soft-robotic ray. *Science* **353**, 158–162 (2016).
13. K. Saito, K. Iwata, Y. Ishihara, K. Sugita, M. Takato, F. Uchikoba, Miniaturized rotary actuators using shape memory alloy for insect-type MEMS microrobot. *Micromachines* **7**, 58 (2016).
14. K. Sugita, T. Tanaka, Y. Nakata, M. Takato, K. Saito, F. Uchikoba, Hexapod type MEMS microrobot equipped with an artificial neural networks IC. *J. Robot. Netw. Artif. Life* **4**, 28–31 (2017).
15. R. K. Josephson, J. G. Malamud, D. R. Stokes, Power output by an asynchronous flight muscle from a beetle. *J. Exp. Biol.* **203**, 2667–2689 (2000).
16. W. Lai, C. K. Erdonmez, T. F. Marinis, C. K. Bjune, N. J. Dudney, F. Xu, R. Wartena, Y.-M. Chiang, Ultrahigh-energy-density microbatteries enabled by new electrode architecture and micropackaging design. *Adv. Mater.* **22**, E139–E144 (2010).
17. M. J. Klowden, *Physiological Systems in Insects* (Academic Press, ed. 3, 2013).
18. E. L. Arrese, J. L. Soulages, Insect fat body: Energy, metabolism, and regulation. *Annu. Rev. Entomol.* **55**, 207–225 (2010).
19. V. H. Ebron, Z. Yang, D. J. Seyer, M. E. Kozlov, J. Oh, H. Xie, J. Razal, L. J. Hall, J. P. Ferraris, A. G. MacDiarmid, R. H. Baughman, Fuel-powered artificial muscles. *Science* **311**, 1580–1583 (2006).
20. J. D. Madden, Artificial muscle begins to breathe. *Science* **311**, 1559–1560 (2006).
21. H. Bateman, The control of an elastic fluid. *Bull. Amer. Math. Soc.* **51**, 601–646 (1945).
22. K. Xu, N. O. Pérez-Arancibia, Electronics-free logic circuits for localized feedback control of multi-actuator soft robots. *IEEE Robot. Autom. Lett.* **5**, 3990–3997 (2020).
23. C. M. Wayman, Some applications of shape-memory alloys. *JOM* **32**, 129–137 (1980).
24. K. Sun, T.-S. Wei, B. Y. Ahn, J. Y. Seo, S. J. Dillon, J. A. Lewis, 3D printing of interdigitated Li-ion microbattery architectures. *Adv. Mater.* **25**, 4539–4543 (2013).
25. M. Wehner, R. L. Truby, D. J. Fitzgerald, B. Mosadegh, G. M. Whitesides, J. A. Lewis, R. J. Wood, An integrated design and fabrication strategy for entirely soft, autonomous robots. *Nature* **536**, 451 (2016).
26. X. Chen, D. Goodnight, Z. Gao, A. H. Cavusoglu, N. Sabharwal, M. DeLay, A. Driks, O. Sahin, Scaling up nanoscale water-driven energy conversion into evaporation-driven engines and generators. *Nat. Commun.* **6**, 7346 (2015).
27. R. J. Wood, The first takeoff of a biologically inspired at-scale robotic insect. *IEEE Trans. Robot.* **24**, 341–347 (2008).
28. R. J. Wood, S. Avadhanula, R. Sahai, E. Steltz, R. S. Fearing, Microrobot design using fiber reinforced composites. *J. Mech. Des.* **130**, 052304 (2008).
29. R. Kraehnert, M. Baerns, Morphology changes of Pt-foil catalyst induced by temperature-controlled ammonia oxidation near atmospheric pressure. *Appl. Catal. A Gen.* **327**, 73–81 (2007).
30. M. T. Janicke, H. Kestenbaum, U. Hagendorf, F. Schüth, M. Fichtner, K. Schubert, The controlled oxidation of hydrogen from an explosive mixture of gases using a microstructured reactor/heat exchanger and Pt/Al_2O_3 catalyst. *J. Catal.* **191**, 282–293 (2000).
31. J. M. Jani, M. Leary, A. Subic, M. A. Gibson, A review of shape memory alloy research, applications and opportunities. *Mater. Des.* **56**, 1078–1113 (2014).
32. L. F. Toledo, J. Z. Ge, J. M. Oxoby, Y. Chen, N. O. Pérez-Arancibia, System identification of a NiTi-based SMA actuator using a modified Preisach model and adaptive control, in *Proceedings of the 2017 American Control Conference (ACC)*, Seattle, WA, 24 to 26 May 2017 (IEEE, 2017), pp. 183–190.
33. J. Z. Ge, L. Chang, N. O. Pérez-Arancibia, Position control of a shape-memory alloy actuator using a Preisach-model-based inverse-temperature method, in *Proceedings of the 2019 American Control Conference (ACC)*, Philadelphia, PA, 10 to 12 July 2019 (IEEE, 2019), pp. 3801–3808.
34. D. J. Leo, *Engineering Analysis of Smart Material Systems* (John Wiley & Sons, 2007).
35. D. C. Lagoudas, *Shape Memory Alloys: Modeling and Engineering Applications* (Springer Science & Business Media, 2008).
36. J.-S. Koh, E. Yang, G.-P. Jung, S.-P. Jung, J. H. Son, S.-I. Lee, P. G. Jablonski, R. J. Wood, H.-Y. Kim, K.-J. Cho, Jumping on water: Surface tension-dominated jumping of water striders and robotic insects. *Science* **349**, 517–521 (2015).
37. Z. Wang, G. Hang, J. Li, Y. Wang, K. Xiao, A micro-robot fish with embedded SMA wire actuated flexible biomimetic fin. *Sens. Actuators A Phys.* **144**, 354–360 (2008).
38. M. Kovac, A. Guignard, J.-D. Nicoud, J.-C. Zufferey, D. Floreano, A 1.5g SMA-actuated microglider looking for the light, in *Proceedings of the 2007 IEEE International Conference on Robotics and Automation (ICRA)*, Rome, Italy, 10 to 14 April 2007 (IEEE, 2007), pp. 367–372.
39. R. Srinivasan, I.-M. Hsing, P. E. Berger, K. F. Jensen, S. L. Firebaugh, M. A. Schmidt, M. P. Harold, J. J. Lerou, J. F. Ryley, Micromachined reactors for catalytic partial oxidation reactions. *AIChE J.* **43**, 3059–3069 (1997).
40. R. Dudley, *The Biomechanics of Insect Flight* (Princeton Univ. Press, 2000).
41. K. Y. Ma, "Mechanical design and manufacturing of an insect-scale flapping-wing robot," thesis, Harvard University, Cambridge, MA (2015).
42. B. M. Finio, N. O. Pérez-Arancibia, R. J. Wood, System identification and linear time-invariant modeling of an insect-sized flapping-wing micro air vehicle, in *Proceedings of the 2011 IEEE/RSJ International Conference on Intelligent Robots and Systems (IROS)*, San Francisco, CA, 25 to 30 September 2011 (IEEE, 2011), pp. 1107–1114.
43. P. Bußhardt, S. N. Gorb, Walking on smooth and rough ground: Activity and timing of the claw retractor muscle in the beetle *Pachnoda marginata peregrina* (Coleoptera, Scarabaeidae). *J. Exp. Biol.* **216**, 319–328 (2013).
44. M. Calisti, G. Picardi, C. Laschi, Fundamentals of soft robot locomotion. *J. R. Soc. Interface* **14**, 20170101 (2017).
45. J. Z. Ge, A. A. Calderón, N. O. Pérez-Arancibia, An earthworm-inspired friction-controlled soft robot capable of bidirectional locomotion. *Bioinspir. Biomim.* **14**, 036004 (2019).
46. J.-S. Koh, K.-J. Cho, Omega-shaped inchworm-inspired crawling robot with large-index-and-pitch (LIP) SMA spring actuators. *IEEE ASME Trans. Mechatron.* **18**, 419–429 (2013).
47. H.-Y. Yu, J.-J. Chen, T.-R. Hsiang, Design and implementation of a real-time object location system based on passive RFID tags. *IEEE Sens. J.* **15**, 5015–5023 (2015).
48. S.-H. Song, J.-Y. Lee, H. Rodrigue, I.-S. Choi, Y. J. Kang, S.-H. Ahn, 35 Hz shape memory alloy actuator with bending-twisting mode. *Sci. Rep.* **6**, 21118 (2016).
49. R. Baughman, Fuel-powered artificial muscles for the robotic soldier (2007); https://www.researchgate.net/publication/235043961_Fuel-Powered_Artificial_Muscles_for_the_Robotic_Soldier.
50. R. H. Baughman, V. H. Ebron, Z. Yang, D. J. Seyer, M. Kozlov, J. Oh, H. Xie, J. Razal, J. P. Ferraris, A. G. MacDiarmid, W. A. Macaulay, Fuel-powered actuators and methods of using same. U.S. Patent 8,096,119 (2012).
51. A. A. Calderón, Y. Chen, X. Yang, L. Chang, X.-T. Nguyen, E. K. Singer, N. O. Pérez-Arancibia, Control of flying robotic insects: A perspective and unifying approach, in *2019 19th International Conference on Advanced Robotics (ICAR)*, Belo Horizonte, Brazil, 2 to 6 December 2019 (IEEE, 2019), pp. 747–754.
52. K. Farahmand, J. W. Kaufman, Experimental measurement of fine thermocouple response time in air. *Exp. Heat Transfer* **14**, 107–118 (2001).
53. Y. A. Çengel, A. Ghajar, *Heat and Mass Transfer: Fundamentals and Applications* (McGraw-Hill, ed. 5, 2015).
54. Y. A. Çengel, M. A. Boles, *Thermodynamics: An Engineering Approach* (McGraw-Hill, ed. 4, 2002).
55. X. Ji, X. Liu, V. Cacucciolo, M. Imboden, Y. Civet, A. El Haitami, S. Cantin, Y. Perriard, H. Shea, An autonomous untethered fast soft robotic insect driven by low-voltage dielectric elastomer actuators. *Sci. Robot.* **4**, eaaz6451 (2019).
56. A. M. Hoover, E. Steltz, R. S. Fearing, RoACH: An autonomous 2.4g crawling hexapod robot, in *Proceedings of the 2008 IEEE/RSJ International Conference on Intelligent Robots and Systems (IROS)*, Nice, France, 22 to 26 September 2008 (IEEE, 2008), pp. 26–33.
57. Z. Dai, S. N. Gorb, U. Schwarz, Roughness-dependent friction force of the tarsal claw system in the beetle *Pachnoda marginata* (Coleoptera, Scarabaeidae). *J. Exp. Biol.* **205**, 2479–2488 (2002).
58. B. Shin, J. Ha, M. Lee, K. Park, G. H. Park, T. H. Choi, K.-J. Cho, H.-Y. Kim, Hygrobot: A self-locomotive ratcheted actuator powered by environmental humidity. *Sci. Robot.* **3**, eaar2629 (2018).
59. C. A. Balanis, *Antenna Theory: Analysis and Design* (John Wiley & Sons, 2016).
60. B. Goldberg, R. Zufferey, N. Doshi, E. F. Helbling, G. Whittredge, M. Kovac, R. J. Wood, Power and control autonomy for high-speed locomotion with an insect-scale legged robot. *IEEE Robot. Autom. Lett.* **3**, 987–993 (2018).

61. M. Goldfarb, M. Gogola, G. Fischer, E. Garcia, Development of a piezoelectrically-actuated mesoscale robot quadruped. *J. Micromechatronics* **1**, 205–219 (2001).
62. M. Rubenstein, C. Ahler, R. Nagpal, Kilobot: A low cost scalable robot system for collective behaviors, in *Proceedings of the 2012 IEEE International Conference on Robotics and Automation (ICRA)*, Saint Paul, MN, 14 to 18 May 2012 (IEEE, 2012), pp. 3293–3298.
63. M. Qi, Y. Zhu, Z. Liu, X. Zhang, X. Yan, L. Lin, A fast-moving electrostatic crawling insect, in *Proceedings of the 2017 IEEE 30th International Conference on Micro Electro Mechanical Systems (MEMS)*, Las Vegas, NV, 22 to 26 January 2017 (IEEE, 2017), pp. 761–764.
64. D. Avraham, E. Faran, D. Shilo, Self-propagating miniature device based on shape memory alloy. *J. Phys. Commun.* **2**, 015015 (2018).
65. A. T. Baisch, P. S. Sreetharan, R. J. Wood, Biologically-inspired locomotion of a 2g hexapod robot, in *Proceedings of the 2010 IEEE/RSJ International Conference on Intelligent Robots and Systems (IROS)*, Taipei, Taiwan, 18 to 22 October 2010 (IEEE, 2010), pp. 5360–5365.
66. T. Ebefors, J. U. Mattsson, E. Kälvesten, G. Stemme, A walking silicon micro-robot, in *Proceedings of the 10th International Conference on Solid-State Sensors and Actuators (Transducers'99)*, Sendai, Japan, 7 to 10 June 1999 (Elsevier, 1999), pp. 1202–1205.
67. D. L. Christensen, E. W. Hawkes, S. A. Suresh, K. Ladenheim, M. R. Cutkosky, μTugs: Enabling microrobots to deliver macro forces with controllable adhesives, in *Proceedings of the 2015 IEEE International Conference on Robotics and Automation (ICRA)*, Seattle, WA, 26 to 30 May 2015 (IEEE, 2015), pp. 4048–4055.
68. F. Arvin, J. Murray, C. Zhang, S. Yue, Colias: An autonomous micro robot for swarm robotic applications. *Int. J. Adv. Robot. Syst.* **11**, 113 (2014).
69. J. McLurkin, A. J. Lynch, S. Rixner, T. W. Barr, A. Chou, K. Foster, S. Bilstein, A low-cost multi-robot system for research, teaching, and outreach, in *Distributed Autonomous Robotic Systems* (Springer, 2013), pp. 597–609.
70. F. Arvin, K. Samsudin, A. R. Ramli, Development of a miniature robot for swarm robotic application. *Int. J. Comput. Electr. Eng.* **1**, 436–442 (2009).
71. F. Mondada, M. Bonani, X. Raemy, J. Pugh, C. Cianci, A. Klaptocz, S. Magnenat, J.-C. Zufferey, D. Floreano, A. Martinoli, P. J. S. Gonçalves, P. J. D. Torres, C. M. O. Alves, The e-puck, a robot designed for education in engineering, in *Proceedings of the 9th Conference on Autonomous Robot Systems and Competitions* (Instituto Politécnico de Castelo Branco, 2009), vol. 1, pp. 59–65.
72. G. Caprari, "Autonomous micro-robots: Applications and limitations," thesis, EPFL, Lausanne, Switzerland (2003).
73. R. H. Byrne, D. R. Adkins, S. E. Eskridge, J. J. Harrington, E. J. Heller, J. E. Hurtado, Miniature mobile robots for plume tracking and source localization research. *J. Micromechatronics* **1**, 253–261 (2001).
74. J. McLurkin, *Using Cooperative Robots for Explosive Ordnance Disposal* (Massachusetts Institute of Technology Artificial Intelligence Laboratory, 1996), pp. 1–10.
75. M. Asadpour, R. Siegwart, Compact Q-learning optimized for micro-robots with processing and memory constraints. *Robot. Auton. Syst.* **48**, 49–61 (2004).
76. N. Mitsumoto, T. Fukuda, K. Shimojima, A. Ogawa, Micro autonomous robotic system and biologically inspired immune swarm strategy as a multi agent robotic system, in *Proceedings of the 1995 IEEE International Conference on Robotics and Automation (ICRA)*, vol. 2, Nagoya, Japan, 21 to 27 May 1995 (IEEE, 1995), pp. 2187–2192.
77. P. Dario, M. C. Carrozza, C. Stefanini, S. D'Attanasio, A mobile microrobot actuated by a new electromagnetic wobble micromotor. *IEEE ASME Trans. Mechatron.* **3**, 9–16 (1998).
78. J. A. Smith, I. Poulakakis, M. Trentini, I. Sharf, Bounding with active wheels and liftoff angle velocity adjustment. *Int. J. Robot. Res.* **29**, 414–427 (2010).
79. M. Raibert, K. Blankespoor, G. Nelson, R. Playter, Bigdog, the rough-terrain quadruped robot. *IFAC Proc. Vol.* **41**, 10822–10825 (2008).
80. S. Rutishauser, A. Sprowitz, L. Righetti, A. J. Ijspeert, Passive compliant quadruped robot using central pattern generators for locomotion control, in *Proceedings of the 2008 2nd IEEE RAS & EMBS International Conference on Biomedical Robotics and Biomechatronics*, Scottsdale, AZ, 19 to 22 October 2008 (IEEE, 2008), pp. 710–715.
81. H. Kimura, Y. Fukuoka, A. H. Cohen, Adaptive dynamic walking of a quadruped robot on natural ground based on biological concepts. *Int. J. Robot. Res.* **26**, 475–490 (2007).
82. I. Poulakakis, J. A. Smith, M. Buehler, Modeling and experiments of untethered quadrupedal running with a bounding gait: The scout II robot. *Int. J. Robot. Res.* **24**, 239–256 (2005).
83. F. Iida, G. Gómez, R. Pfeifer, Exploiting body dynamics for controlling a running quadruped robot, in *Proceedings of the 2005 IEEE International Conference on Robotics and Automation (ICRA)*, Seattle, WA, 18 to 20 July 2005 (IEEE, 2005), pp. 229–235.
84. A. Spröwitz, A. Tuleu, M. Vespignani, M. Ajallooeian, E. Badri, A. J. Ijspeert, Towards dynamic trot gait locomotion: Design, control, and experiments with Cheetah-cub, a compliant quadruped robot. *Int. J. Robot. Res.* **32**, 932–950 (2013).
85. F. Iida, R. Pfeifer, Cheap rapid locomotion of a quadruped robot: Self-stabilization of bounding gait, in *Intelligent Autonomous Systems* (IOS Press, 2004), vol. 8, pp. 642–649.
86. C. Semini, N. G. Tsagarakis, E. Guglielmino, M. Focchi, F. Cannella, D. G. Caldwell, Design of HyQ–a hydraulically and electrically actuated quadruped robot. *Proc. Inst. Mech. Eng. Pt. I J. Syst. Contr. Eng.* **225**, 831–849 (2011).
87. Y. Fukuoka, H. Kimura, Dynamic locomotion of a biomorphic quadruped 'Tekken' robot using various gaits: Walk, trot, free-gait and bound. *Appl. Bionics Biomech.* **6**, 743713 (2009).
88. Z. G. Zhang, H. Kimura, Rush: A simple and autonomous quadruped running robot. *Proc. Inst. Mech. Eng. Pt. I J. Syst. Contr. Eng.* **223**, 323–336 (2009).
89. J. Estremera, K. J. Waldron, Thrust control, stabilization and energetics of a quadruped running robot. *Int. J. Robot. Res.* **27**, 1135–1151 (2008).
90. Y. Fukuoka, H. Kimura, A. H. Cohen, Adaptive dynamic walking of a quadruped robot on irregular terrain based on biological concepts. *Int. J. Robot. Res.* **22**, 187–202 (2003).
91. M. H. Raibert, Trotting, pacing and bounding by a quadruped robot. *J. Biomech.* **23**, 79–98 (1990).
92. M. T. Tolley, R. F. Shepherd, B. Mosadegh, K. C. Galloway, M. Wehner, M. Karpelson, R. J. Wood, G. M. Whitesides, A resilient, untethered soft robot. *Soft Robot.* **1**, 213–223 (2014).
93. C. D. Onal, D. Rus, Autonomous undulatory serpentine locomotion utilizing body dynamics of a fluidic soft robot. *Bioinspir. Biomim.* **8**, 026003 (2013).
94. B. Kim, M. G. Lee, Y. P. Lee, Y. Kim, G. Lee, An earthworm-like micro robot using shape memory alloy actuator. *Sens. Actuator A Phys.* **125**, 429–437 (2006).
95. J. Ning, C. Ti, Y. Liu, Inchworm inspired pneumatic soft robot based on friction hysteresis. *J. Robot. Autom.* **1**, 54–63 (2017).
96. C. T. Nguyen, H. Phung, H. Jung, U. Kim, T. D. Nguyen, J. Park, H. Moon, J. C. Koo, H. R. Choi, Printable monolithic hexapod robot driven by soft actuator, in *Proceedings of the 2015 IEEE International Conference on Robotics and Automation (ICRA)*, Seattle, WA, 26 to 30 May 2015 (IEEE, 2015), pp. 4484–4489.
97. W. Wang, J.-Y. Lee, H. Rodrigue, S.-H. Song, W.-S. Chu, S.-H. Ahn, Locomotion of inchworm-inspired robot made of smart soft composite (SSC). *Bioinspir. Biomim.* **9**, 046006 (2014).
98. S. W. Kwok, S. A. Morin, B. Mosadegh, J.-H. So, R. F. Shepherd, R. V. Martinez, B. Smith, F. C. Simeone, A. A. Stokes, G. M. Whitesides, Magnetic assembly of soft robots with hard components. *Adv. Funct. Mater.* **24**, 2180–2187 (2014).
99. S. Ueno, K. Takemura, S. Yokota, K. Edamura, Micro inchworm robot using electro-conjugate fluid. *Sens. Actuator A Phys.* **216**, 36–42 (2014).
100. D. Morales, E. Palleau, M. D. Dickey, O. D. Velev, Electro-actuated hydrogel walkers with dual responsive legs. *Soft Matter* **10**, 1337–1348 (2014).
101. Y. Ma, Y. Zhang, B. Wu, W. Sun, Z. Li, J. Sun, Polyelectrolyte multilayer films for building energetic walking devices. *Angew. Chem.* **123**, 6378–6381 (2011).
102. N. Tomita, K. Takagi, K. Asaka, Development of a quadruped soft robot with fully IPMC body, in *Proceedings of the SICE Annual Conference 2011*, Tokyo, Japan, 13 to 18 September 2011 (IEEE, 2011), pp. 1687–1690.
103. N. Cheng, G. Ishigami, S. Hawthorne, H. Chen, M. Hansen, M. Telleria, R. Playter, K. Iagnemma, Design and analysis of a soft mobile robot composed of multiple thermally activated joints driven by a single actuator, in *Proceedings of the 2010 IEEE International Conference on Robotics and Automation (ICRA)*, Anchorage, AK, 3 to 7 May 2010 (IEEE, 2010), pp. 5207–5212.
104. S. Guo, L. Shi, K. Asaka, IPMC actuator-based an underwater microrobot with 8 legs, in *Proceedings of the 2008 IEEE International Conference on Mechatronics and Automation*, Takamatsu, Japan, 5 to 8 August 2008 (IEEE, 2008), pp. 551–556.
105. L. Shi, S. Guo, K. Asaka, S. Mao, Development and experiments of a novel multifunctional underwater microrobot, in *Proceedings of the 2010 IEEE International Conference on Nano/Molecular Medicine and Engineering*, Hong Kong/Macau, China, 5 to 9 December 2010 (IEEE, 2010), pp. 1–6.
106. K. Jung, J. C. Koo, Y. K. Lee, H. R. Choi, Artificial annelid robot driven by soft actuators. *Bioinspir. Biomim.* **2**, S42–S49 (2007).
107. W. Zhang, S. Guo, K. Asaka, Development of an underwater biomimetic microrobot with compact structure and flexible locomotion. *Microsyst. Technol.* **13**, 883–890 (2007).
108. S. Maeda, Y. Hara, T. Sakai, R. Yoshida, S. Hashimoto, Self-walking gel. *Adv. Mater.* **19**, 3480–3484 (2007).
109. Y. Wu, J. K. Yim, J. Liang, Z. Shao, M. Qi, J. Zhong, Z. Luo, X. Yan, M. Zhang, X. Wang, R. S. Fearing, R. J. Full, L. Lin, Insect-scale fast moving and ultrarobust soft robot. *Sci. Robot.* **4**, eaax1594 (2019).
110. G. A. Bartholomew, J. R. B. Lighton, G. N. Louw, Energetics of locomotion and patterns of respiration in tenebrionid beetles from the Namib Desert. *J. Comp. Physiol. B* **155**, 155–162 (1985).
111. S. Rubin, M. H.-Y. Young, J. C. Wright, D. L. Whitaker, A. N. Ahn, Exceptional running and turning performance in a mite. *J. Exp. Biol.* **219**, 676–685 (2016).
112. F. Punzo, The effects of reproductive status on sprint speed in the solifuge, *Eremobates marathoni* (Solifugae, Eremobatidae). *J. Arachnol.* **26**, 113–116 (1998).
113. G. C. Wu, J. C. Wright, D. L. Whitaker, A. N. Ahn, Kinematic evidence for superfast locomotory muscle in two species of teneriffiid mites. *J. Exp. Biol.* **213**, 2551–2556 (2010).

114. R. J. Full, M. S. Tu, Mechanics of a rapid running insect: Two-, four- and six-legged locomotion. *J. Exp. Biol.* **156**, 215–231 (1991).
115. T. Weihmann, P.-G. Brun, E. Pycroft, Speed dependent phase shifts and gait changes in cockroaches running on substrates of different slipperiness. *Front. Zool.* **14**, 54 (2017).
116. T. F. Jensen, I. Holm-Jensen, Energetic cost of running in workers of three ant species, *Formica fusca* L., *Formica rufa* L., and *Camponotus herculeanus* L. (Hymenoptera, Formicidae). *J. Comp. Physiol.* **137**, 151–156 (1980).
117. F. D. Duncan, R. M. Crewe, A comparison of the energetics of foraging of three species of *Leptogenys* (Hymenoptera, Formicidae). *Physiol. Entomol.* **18**, 372–378 (1993).

Acknowledgments: We thank the Core Center of Excellence in Nano Imaging at USC for their assistance to capture the SEM images shown in the paper. **Funding:** This work was partially supported by the NSF through NRI award 1528110. Additional support was provided by the USC Viterbi School of Engineering through a start-up fund to N.O.P.-A.
Author contributions: X.Y. designed, fabricated, and tested the robot; developed the microfabrication method used to create the NiTi-Pt–based artificial muscles; performed the experiments; analyzed the experimental and simulation data; and wrote the paper. L.C. analyzed the experimental data, developed the dynamical model of locomotion, implemented and performed the numerical simulations, and wrote the paper. N.O.P.-A. conceived the idea of using catalytic combustion–driven NiTi-Pt wires for microrobotic actuation, conceived the idea of using electronics-free mechanical devices to control catalytic combustion, analyzed the experimental and simulation data, directed the research, and wrote and edited the paper. **Competing interests:** The authors declare that they have no competing interests. **Data and materials availability:** All data needed to evaluate the conclusions of the paper are available in the paper or the Supplementary Materials. Source code of simulation is available on GitHub (https://github.com/XiufengYang/beetlesim).

Submitted 27 October 2019
Accepted 15 July 2020
Published 19 August 2020
10.1126/scirobotics.aba0015

Citation: X. Yang, L. Chang, N. O. Pérez-Arancibia, An 88-milligram insect-scale autonomous crawling robot driven by a catalytic artificial muscle. *Sci. Robot.* **5**, eaba0015 (2020).

Science Robotics

An 88-milligram insect-scale autonomous crawling robot driven by a catalytic artificial muscle

Xiufeng Yang, Longlong Chang, and Néstor O. Pérez-Arancibia

Sci. Robot. **5** (45), eaba0015. DOI: 10.1126/scirobotics.aba0015

Science Robotics (ISSN 2470-9476) is published by the American Association for the Advancement of Science. 1200 New York Avenue NW, Washington, DC 20005. The title *Science Robotics* is a registered trademark of AAAS.